

Relativistic Spin Precession in the Double Pulsar

Rene P. Breton,^{1*} Victoria M. Kaspi,¹ Michael Kramer,²
 Maura A. McLaughlin,^{3,4} Maxim Lyutikov,⁵ Scott M. Ransom,⁶
 Ingrid H. Stairs,⁷ Robert D. Ferdman,^{7,8}
 Fernando Camilo⁹, Andrea Possenti¹⁰

¹Department of Physics, McGill University, Montreal, QC H3A 2T8, Canada

²Jodrell Bank Observatory, University of Manchester, Manchester, M13 9PL, UK

³Department of Physics, West Virginia University, Morgantown, WV 26506, USA

⁴National Radio Astronomy Observatory, Green Bank, WV 24944, USA

⁵Department of Physics, Purdue University, West Lafayette, IN 47907, USA

⁶National Radio Astronomy Observatory, Charlottesville, VA 22903, USA

⁷Department of Physics and Astronomy, University of British Columbia,
 Vancouver, BC V6T 1Z1, Canada

⁸LPCE / CNRS, F-45071 Orleans cedex 2, France

⁹Columbia Astrophysics Laboratory, Columbia University, New York, NY 10027, USA

¹⁰INAF - Osservatorio Astronomico di Cagliari, Poggio dei Pini, 09012 Capoterra, Italy

*To whom correspondence should be addressed; E-mail: bretonr@physics.mcgill.ca.

The double pulsar PSR J0737–3039A/B consists of two neutron stars in a highly relativistic orbit that displays a roughly 30-second eclipse when pulsar A passes behind pulsar B. Describing this eclipse of pulsar A as due to absorption occurring in the magnetosphere of pulsar B, we successfully use a simple geometric model to characterize the observed changing eclipse morphology and to measure the relativistic precession of pulsar B’s spin axis around the total orbital angular momentum. This provides a test of general relativity

and alternative theories of gravity in the strong-field regime. Our measured relativistic spin precession rate of $4.77^{+0.66}_{-0.65} \text{ }^\circ\text{yr}^{-1}$ (68% confidence level) is consistent with that predicted by general relativity within an uncertainty of 13%.

Spin is a fundamental property of most astrophysical bodies, making the study of its gravitational interaction an important challenge (1). Spin interaction manifests itself in different forms. For instance, we expect the spin of a compact rotating body in a binary system with another compact companion to couple gravitationally with the orbital angular momentum (relativistic spin-orbit coupling) and also with the spin of this companion (relativistic spin-spin coupling) (2, 3). Observing such phenomena provides important tests for theories of gravity, because every successful theory must be able to describe the couplings and to predict their observational consequences. In a binary system consisting of compact objects such as neutron stars, one can generally consider the spin-orbit contribution acting on each body to dominate greatly the spin-spin contribution. This interaction results in a precession of the bodies' spin axis around the orbital angular momentum of the system, behavior we refer to as *relativistic spin precession*.

While relativistic spin precession is well studied theoretically in general relativity (GR), the same is not true of alternative theories of gravity and hence, quantitative predictions of deviations from GR spin precession do not yet exist (2). For instance, it is expected that in alternative theories relativistic spin precession may also depend on strong self-gravitational effects, i.e. the actual precession may depend on the structure of a gravitating body (2). In the weak gravitational fields encountered in the solar system, these strong-field effects generally cannot be detected (5, 6, 7). Measurements in the strong-field regime near massive and compact bodies such as neutron stars and black holes are required. Relativistic spin precession has been observed in some binary pulsars [e.g. (8, 9, 10)], but it has usually only provided a qualitative confirmation of the effect. Recently, the binary pulsar PSR B1534+12 has allowed the first

quantitative measurement of this effect in a strong field, and although the spin precession rate was measured to low precision, it was consistent with the predictions of GR (*11*).

Here we report a precision measurement of relativistic spin precession using eclipses observed in the double pulsar (*12, 13*). This measurement, combined with observational access to both pulsar orbits in this system, allows us to constrain quantitatively relativistic spin precession in the strong-field regime within a general class of gravitational theories that includes GR.

PSR J0737–3039A/B consists of two neutron stars, both visible as radio pulsars, in a relativistic 2.45-hour orbit (*12, 13*). High-precision timing of the pulsars, having spin periods of 23 ms and 2.8 s (hereafter called pulsars A and B, respectively), has already proven to be the most stringent test-bed for GR in the strong-field regime (*14*), and enables four independent timing tests of gravity, more than any other binary system.

The orbital inclination of the double pulsar system is such that we observe the system almost perfectly edge-on. This coincidence causes pulsar A to be eclipsed by pulsar B at pulsar A’s superior conjunction (*13*). The modestly frequency-dependent eclipse duration, about 30 s, corresponds to a region extending $\sim 1.5 \times 10^7$ m (*15*). The light curve of pulsar A during its eclipse shows flux modulations that are spaced by half or integer numbers of pulsar B’s rotational period (*16*). This indicates that the material responsible for the eclipse corotates with pulsar B. The relative orbital motions of the two pulsars and the rotation of pulsar B thus allow a probe of different regions of pulsar B’s magnetosphere in a plane containing the line of sight and the orbital motion.

Synchrotron resonance with relativistic electrons is the most likely mechanism for efficient absorption of radio emission over a wide range of frequencies. In the model proposed by Lyutikov and Thompson (*1*), this absorbing plasma corotates with pulsar B and is confined within the closed field lines of a magnetic dipole truncated by the relativistic wind of pulsar A. The dipole magnetic moment vector makes an angle α with respect to the spin axis of pulsar B,

whose orientation in space can be described by two angles: the colatitude of the spin axis with respect to the total angular momentum of the system, θ , and the longitude of the spin axis, ϕ (see Fig. 1 for an illustration of the system geometry). Additional parameters characterizing the plasma opacity, μ , the truncation radius of the magnetosphere, R_{mag} , and the relative position of pulsar A with respect to the projected magnetosphere of pulsar B, z_0 , are also included in the model (1).

We monitored the double pulsar from December 2003 to November 2007 using the Green Bank Telescope in West Virginia; most of the data were acquired as part of the timing observations reported in (14). The data used for our analysis were taken at 820 MHz with the SPIGOT instrument (18), which provides 1024 frequency channels across a 50 MHz bandwidth. Data for a total of 63 eclipses of pulsar A were collected over the 4-year period, with many obtained during semi-annual concentrated observing campaigns. We dedispersed each eclipse data set by adding time shifts to frequency channels in order to compensate for the frequency-dependent travel time of radio waves in the ionized interstellar medium and we then folded them at the predicted spin period of pulsar A using the pulsar analysis packages PRESTO (19) and SIGPROC (20) (see (14) for details about the radio timing). Next, we extracted the relative pulsed flux density of pulsar A by fitting each folded interval for the amplitude of a high signal-to-noise ratio pulse profile template made from the integrated pulse observed during the several-hour observation that includes each eclipse. Finally, we normalized the flux densities so the average level outside the eclipse region corresponded to unity. We chose the time resolution of our eclipse light curves to equal, on average, four individual pulses of pulsar A (~ 91 ms).

In addition to the flux density, we determined the orbital phase and the spin phase of pulsar B corresponding to each data point of our time series. Orbital phases were derived from the ephemeris published in (14). Spin phases were empirically measured from data folded at the predicted period of pulsar B in a way similar to that described above for pulsar A. Over the four-

year monitoring campaign, we found significant changes in pulsar B’s pulse profile, likely due to the precession of its spin axis, which were also reported in (21). Around 2003, the average pulse profile was unimodal, resembling a Gaussian function. It evolved such that by 2007, it displayed two narrow peaks. Using the pulse peak maximum as a fiducial reference point is certainly not appropriate. We find, however, that the unimodal profile gradually became wider and then started to form a gap near the center of its peak. Since then, the outer edges of the pulse profile have not significantly changed but the gap evolved such that two peaks are now visible. This lets us presume that the underlying average profile is reminiscent of a Gaussian-like profile to which some “absorption” feature has been superimposed near the center, leaving a narrow peak on each side. We therefore defined the fiducial reference point to lie at the center of the unimodal “envelope” that we reconstructed from the first ten Fourier bins of the pulse profile, which contains 512 bins in total (see Fig. S2 of the Supporting Online Material for an illustration of the pulse profile evolution).

We implemented the eclipse modeling of our data in two steps: the fitting of individual eclipse profiles and the search for evolution of the geometry of pulsar B. We first searched the full phase space to identify best-fit values of six parameters (see Supporting Online Material for more details). Then, we reduced the number of free parameters to the subset (θ, ϕ, α) describing the orientation of pulsar B’s spin and magnetic axes by fixing the other parameters to their best-fit values: $\mu = 2$, $R_{\text{mag}} = 1.29^\circ$ (projected value in terms of orbital phase) and $z_0/R_{\text{mag}} = -0.543$ (see Fig. 1). Finally, we performed a high-resolution mapping of the likelihood of this subspace in order to investigate subtle changes in the geometry. Lyutikov and Thompson (1) predicted that such changes, due to relativistic spin precession, could affect the eclipse light curve. In principle, relativistic spin precession of pulsar B’s spin axis around the total angular momentum should induce a secular change of the longitude of the spin axis, ϕ , while the magnetic inclination, α , and the colatitude of the spin axis, θ , are expected to remain fixed

over time. Indeed, from model fitting, we find no significant time evolution of α and θ , whereas ϕ does change. Because of correlation between the parameters, we jointly evaluated the best-fit geometry of pulsar B using a time-dependent model in which $\alpha = \alpha_0$ and $\theta = \theta_0$ are constants, and ϕ varies linearly with time, i.e. $\phi = \phi_0 - \Omega_B t$, where Ω_B is the rate of change of pulsar B's spin axis longitude and the epoch of $\phi = \phi_0$ is May 2, 2006 (MJD 53857). Figure 2 shows the time evolution of the parameters and the fit derived from this joint time-dependent model (Table 1). The precession rate Ω_B of $4.77^{+0.66}_{-0.65} \text{ }^\circ \text{yr}^{-1}$ (22) agrees with the precession rate predicted by GR (23), $5.0734 \pm 0.0007 \text{ }^\circ \text{yr}^{-1}$ (24), within an uncertainty of 13% (68% confidence level).

This relatively simple model (*I*) is able to reproduce the complex phenomenology of the eclipses (see Fig. 3 and Movie S1 in Supporting Online Material) except at the eclipse boundaries where slight magnetospheric distortions or variations in plasma density are likely to occur. Fits including the egress generally are poor in the central region where we observe narrow modulation features, which are critical for determining pulsar B's geometry. For this reason, we excluded the egress from the fits, using orbital phases between -1.0 and 0.75° (see Fig. 3). We accounted for systematics introduced by the choice of the region to fit in the priors of our Bayesian model (see Supporting Online Material). This improved the fit of the model throughout the center region of the eclipse while still producing qualitatively good predictions near the eclipse egress. The overall success of the model implies that the geometry of pulsar B's magnetosphere is accurately described as predominantly dipolar; a pure quadrupole, for instance, does not reproduce the observed light curves. Although the model does not exclude the possibility that higher-order multipole components may exist close to the surface of pulsar B, our modeling supports the conclusions (*I*) that these eclipses yield direct empirical evidence supporting the long-standing assumption that pulsars have mainly dipolar magnetic fields far from their surface.

The direct outcome from modeling the eclipse profile evolution is a measurement of the effect of relativistic spin precession (see Movie S2 in Supporting Online Material for an illustration of the time evolution of the eclipse). We can use the inferred precession rate to test GR (see Fig. 4) and to further constrain alternative theories of gravity and the strong-field aspects of relativistic spin precession. We use the generic class of relativistic theories that are fully conservative (Lorentz-invariant) and based on a Lagrangian, as introduced by Damour & Taylor (2). In this way we can study the constraints of our observations on theories of gravity by describing the spin-orbit interaction within a specific theory by coupling functions appearing in the corresponding part of the Lagrangian. In this framework, we can write the precession rate of pulsar B in a general form, $\Omega_B = \sigma_B L / a_R^3 (1 - e^2)^{3/2}$ where L is the orbital angular momentum of the system, a_R is the semimajor axis of the relative orbit between the pulsars, e the eccentricity of the orbit and σ_B is a generic strong-field spin-orbit coupling constant. Since L and a_R are not directly measurable, it is more convenient to write the above expression using observable Keplerian and post-Keplerian parameters. While alternative forms generally involve a mixture of gravitational theory-dependent terms, the particular choice $\Omega_B = \frac{x_A x_B}{s^2} \times \frac{n^3}{1-e^2} \times \frac{c^2 \sigma_B}{\mathcal{G}}$ is the only one that does not incorporate further theoretical terms other than the spin-orbit coupling constant, σ_B , the speed of light, c , and a generalized gravitational constant for the interaction between the two pulsars, \mathcal{G} . In this expression, the Keplerian parameters e and $n = 2\pi/P_b$, the angular orbital frequency, are easily measurable for any binary system. On the other hand, the post-Keplerian Shapiro delay shape parameter s , equivalent to the sine of the orbital inclination angle (2), requires relatively edge-on orbits to be observed. Measurement of the projected semi-major axes of the two orbits (25), x_A and x_B , found in the above equation, necessitates that each body must be timeable. Therefore, the double pulsar is the only relativistic binary system that allows a direct constraint on the spin-orbit coupling in general theories of gravity. Using the inferred precession rate of $\Omega_B = 4.77^{+0.66}_{-0.65} \circ$

yr⁻¹, we derive $\left(\frac{c^2\sigma_B}{\mathcal{G}}\right) = 3.38^{+0.49}_{-0.46}$. Every successful theory of gravity in the given generic framework must predict this value — these observations provide a strong-field test of gravity that complements and goes beyond the weak-field tests of relativistic spin precession (26). In GR, we expect to measure $\left(\frac{c^2\sigma_B}{\mathcal{G}}\right)_{\text{GR}} = 2 + \frac{3}{2}\frac{m_A}{m_B} = 3.60677 \pm 0.00035$, where we have used the masses determined from the precisely observed orbital precession and the Shapiro delay shape parameter under the assumption that GR is correct (14). Comparing the observed value with GR’s predictions, we find $\left(\frac{c^2\sigma_B}{\mathcal{G}}\right)_{\text{obs}} / \left(\frac{c^2\sigma_B}{\mathcal{G}}\right)_{\text{GR}} = 0.94 \pm 0.13$. Hence, GR passes this test of relativistic spin precession in a strong-field regime, confirming, within uncertainties, GR’s effacement property of gravity even for spinning bodies, i.e. the notion that strong internal gravitational fields do not prevent a compact rotating body from behaving just like a spinning test particle in an external weak field (27).

The spin precession rate, as well as the timing parameters entering in the calculation of $\left(\frac{c^2\sigma_B}{\mathcal{G}}\right)$, are all independent of the assumed theory of gravity. If the main contribution limiting the precision of this new strong-field test comes from the inferred spin precession rate, we expect that the statistical uncertainty should decrease significantly with time, roughly as the square of the monitoring baseline for similar quantity and quality of eclipse data. The contribution of systematics to the error budget should also decrease, but its functional time dependence is difficult to estimate. Although the orbital and spin phases of pulsar B are input variables to the eclipse model, our ability to determine the orientation of pulsar B in space does not require the degree of high-precision timing needed for measurement of post-Keplerian parameters; evaluating spin phases to the percent-level, for instance, is sufficient. Therefore, the intrinsic correctness of the model and its ability to reproduce future changes in the eclipse profile due to evolution of the geometry are the most likely limitations to improving the quality of this test of gravity, at least until the measured precession rate reaches a precision comparable with the timing parameters involved in the calculation of $\left(\frac{c^2\sigma_B}{\mathcal{G}}\right)$. Better eclipse modeling could be achieved

from more sensitive observations and thus new generation radio telescopes such as the proposed Square Kilometer Array could help make important progress. Pulsar A does not show evidence of precession (28, 29) likely because its spin axis is aligned with the orbital angular momentum; it should therefore always remain visible, thus allowing long-term monitoring of its eclipses. Pulsar B, however, could disappear if spin precession causes its radio beam to miss our line of sight (21). In this event, we would need to find a way to circumvent the lack of observable spin phases for pulsar B, which are necessary to the eclipse fitting.

References and Notes

1. C. Will, *Living Reviews in Relativity* **4**, 4 (2001).
2. The contribution from a classical quadrupolar moment is negligible for compact bodies.
3. R. F. O’Connell, *Experimental Gravitation: Proceedings of Course 56 of the International School of Physics “Enrico Fermi”*, B. Bertotti, ed. (Academic Press, 1974), p. 496.
4. T. Damour, J. H. Taylor, *Phys. Rev. D* **45**, 1840 (1992).
5. T. Damour, G. Esposito-Farèse, *Phys. Rev. D* **46**, 4128 (1992).
6. T. Damour, G. Esposito-Farèse, *Classical and Quantum Gravity* **9**, 2093 (1992).
7. T. Damour, G. Esposito-Farèse, *Phys. Rev. D* **53**, 5541 (1996).
8. J. M. Weisberg, R. W. Romani, J. H. Taylor, *ApJ* **347**, 1030 (1989).
9. M. Kramer, *ApJ* **509**, 856 (1998).
10. A. W. Hotan, M. Bailes, S. M. Ord, *ApJ* **624**, 906 (2005).
11. I. H. Stairs, S. E. Thorsett, Z. Arzoumanian, *Physical Review Letters* **93**, 141101 (2004).

12. M. Burgay, *et al.*, *Nature* **426**, 531 (2003).
13. A. G. Lyne, *et al.*, *Science* **303**, 1153 (2004).
14. M. Kramer, *et al.*, *Science* **314**, 97 (2006).
15. V. M. Kaspi, *et al.*, *ApJ* **613**, L137 (2004).
16. M. A. McLaughlin, *et al.*, *ApJ* **616**, L131 (2004).
17. M. Lyutikov, C. Thompson, *ApJ* **634**, 1223 (2005).
18. D. L. Kaplan, *et al.*, *PASP* **117**, 643 (2005).
19. S. M. Ransom, S. S. Eikenberry, J. Middleditch, *AJ* **124**, 1788 (2002). PRESTO is freely available at <http://www.cv.nrao.edu/~sransom/presto/>.
20. D. R. Lorimer. SIGPROC is freely available at <http://sigproc.sourceforge.net>.
21. M. Burgay, *et al.*, *ApJ* **624**, L113 (2005).
22. Unless otherwise stated, uncertainties are quoted at the 68% confidence level.
23. B. M. Barker, R. F. O’Connell, *Phys. Rev. D* **12**, 329 (1975).
24. The uncertainty on the predicted GR spin precession rate arises because the value depends on the masses of the system, which are determined from two measured post-Keplerian parameters: the Shapiro delay s parameter and the advance of periastron $\dot{\omega}$.
25. The projected semi-major axes are expressed in terms of light-travel time across the orbit.
26. R. F. O’Connell, *ArXiv e-prints: 0804.3806* (2008).

27. T. Damour, *The problem of motion in Newtonian and Einsteinian gravity*. (Three hundred years of gravitation, 1987), pp. 128–198.
28. R. N. Manchester, *et al.*, *ApJ* **621**, L49 (2005).
29. R. D. Ferdman, *et al.*, *40 Years of Pulsars: Millisecond Pulsars, Magnetars and More* (2008), vol. 983 of *American Institute of Physics Conference Series*, pp. 474–478.
30. We thank N. Wex, T. Damour, R. F. O’Connell, R. D. Blandford and W. G. Unruh for stimulating discussions. The National Radio Astronomy Observatory is a facility of the National Science Foundation operated under cooperative agreement by Associated Universities, Inc. This work was supported in part by the NSERC Discovery Grant program, the Canada Foundation for Innovation, the Canadian Institute for Advanced Research, an FQRNT Team Grant, the Canada Research Chair Program, and the McGill University Lorne Trottier Chair in Astrophysics and Cosmology.
31. W. R. Gilks, *Markov Chain Monte Carlo in Practice* (Chapman & Hall/CRC, 1995).
32. S. Kirkpatrick, C. D. Gelatt, M. P. Vecchi, *Science* **220**, 671 (1983).
33. Marginalization is a common technique in Bayesian analysis that consists of integrating the joint posterior probability over the parameters that are not of interest so that it is reduced, in this case, to a one-dimensional probability for the parameter that we wish to consider (6).

Fig. 1 Schematic view of the double pulsar system showing the important parameters for the modeling of pulsar A's eclipse (dimensions and angles are not to scale). Pulsar B is located at the origin of the cartesian coordinate system while the projected orbital motion of pulsar A during its eclipse is parallel to the y axis at a constant z_0 as seen from Earth, which is located toward the positive x axis. Note that since the orbital inclination is almost perfectly edge-on (14), we can approximate the z axis to be coincident with the orbital angular momentum. The spin axis of pulsar B, whose spatial orientation is described by θ and ϕ , is represented by the Ω vector. The magnetic axis of pulsar B corresponds to the μ vector and makes an angle α with respect to Ω . Finally, the absorbing region of the dipolar magnetosphere of pulsar B, truncated at radius R_{mag} , is shown as a shaded red region.

Fig. 2 Evolution of pulsar B's geometry as a function of time. The marginalized posterior probability distribution of the magnetic inclination (α), the colatitude of the spin axis (θ) and the longitude of the spin axis (ϕ) of pulsar B are shown from top to bottom, respectively. For each data point, the circle represents the median value of the posterior probability density while the box and the bar indicate the 1σ and 3σ confidence intervals, respectively. The gray regions are the 3σ confidence regions derived from the joint time-dependent model fitting. Note that for clarity, multiple eclipses are displayed as single data points when observed over an interval of about a week.

Fig. 3 Average eclipse profile of pulsar A consisting of eight eclipses observed at 820 MHz over a five-day period around April 11, 2007 (black line) along with a model eclipse profile (red dashed line). The relative pulsed flux density of pulsar A is normalized so the average level outside the eclipse region is unity. The resolution of each data point is ~ 91 ms while 1° in orbital phase corresponds to 24.5 s. Note that near orbital phase 0.0 the spikes are separated by the spin period of pulsar B.

Fig. 4 Mass-mass diagram illustrating the present tests constraining general relativity in the

double pulsar system. The inset shows an expanded view of the region where the lines intersect. If general relativity is the correct theory of gravity, all lines should intersect at common values of masses. The mass ratio ($R = x_B/x_A$) and five post-Keplerian parameters (s and r , Shapiro delay ‘shape’ and ‘range’; $\dot{\omega}$, periastron advance; \dot{P}_b , orbital period decay due to the emission of gravitational waves; and γ , gravitational redshift and time dilation) were reported in (14). Shaded regions are unphysical solutions since $\sin i \leq 1$, where i is the orbital inclination. In addition to allowing a test of the strong-field parameter $\left(\frac{c^2 \sigma_B}{G}\right)$, the spin precession rate of pulsar B, Ω_B , yields a new constraint on the mass-mass diagram.

Parameter	Mean	Median	68.2% Confidence	99.7% Confidence
α_0	70.92°	70.94°	$[70.49, 71.31]^\circ$	$[69.68, 72.13]^\circ$
θ_0	130.02°	130.02°	$[129.58, 130.44]^\circ$	$[128.79, 131.37]^\circ$
ϕ_0	51.21°	51.20°	$[50.39, 52.03]^\circ$	$[48.80, 53.72]^\circ$
Ω_B	4.77°yr^{-1}	4.76°yr^{-1}	$[4.12, 5.43]^\circ\text{yr}^{-1}$	$[2.89, 6.90]^\circ\text{yr}^{-1}$

Table 1: Geometrical parameters of pulsar B derived from the eclipse model fitting. Note that the presented values include priors related to systematic uncertainties. The epoch of $\phi = \phi_0$ is May 2, 2006 (MJD 53857).

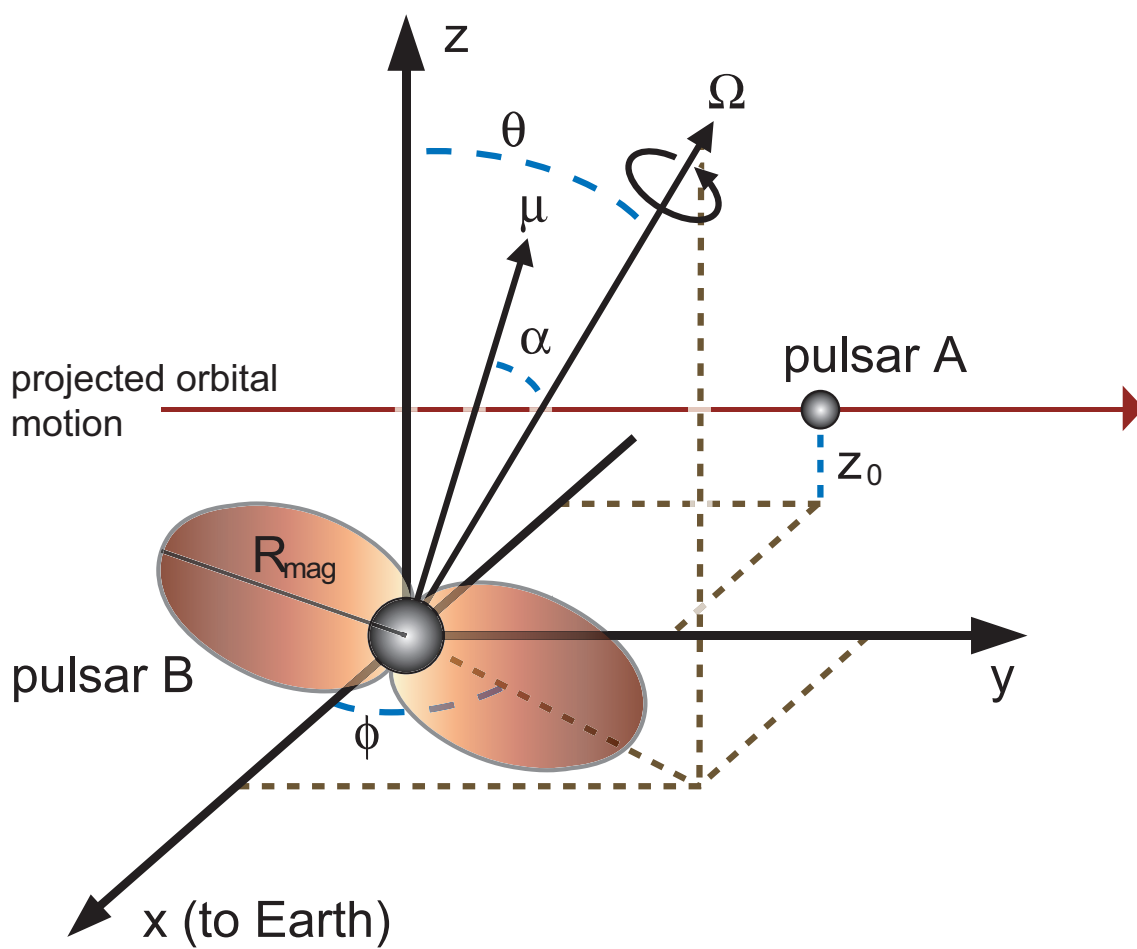


Fig. 1

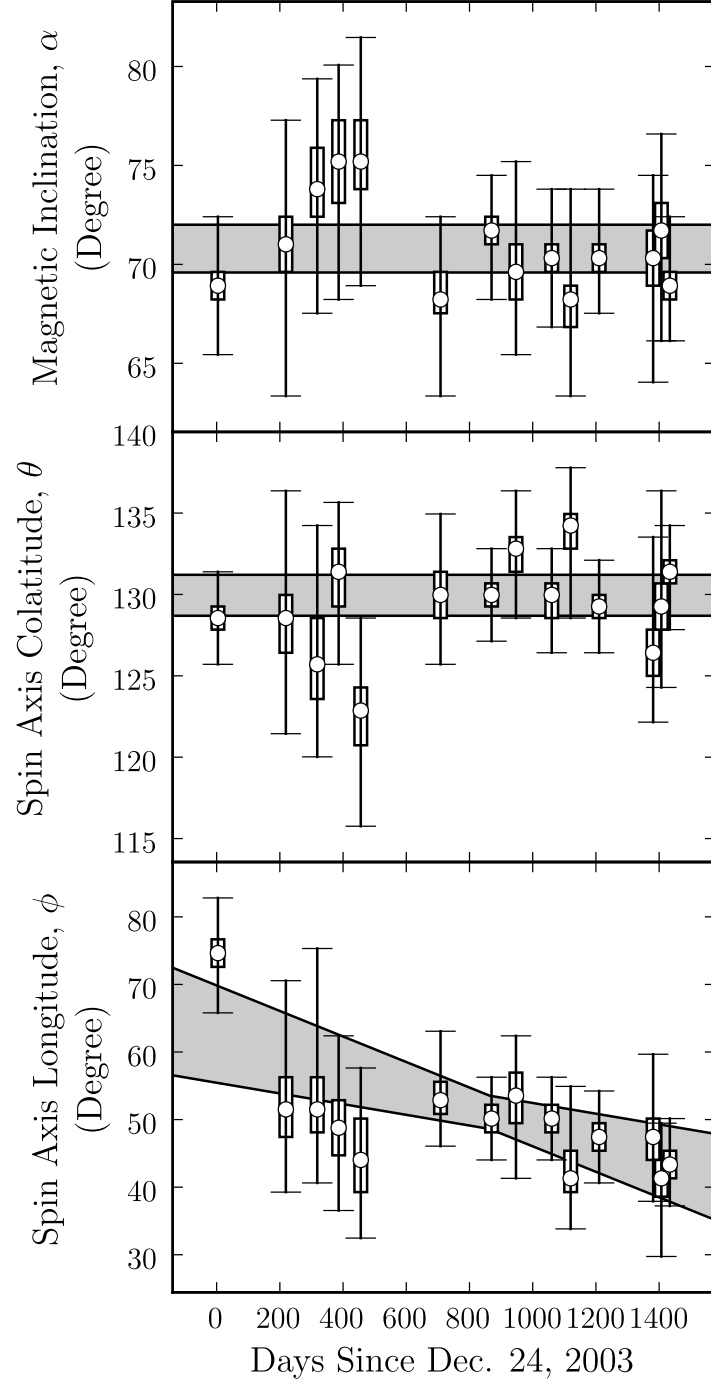


Fig. 2

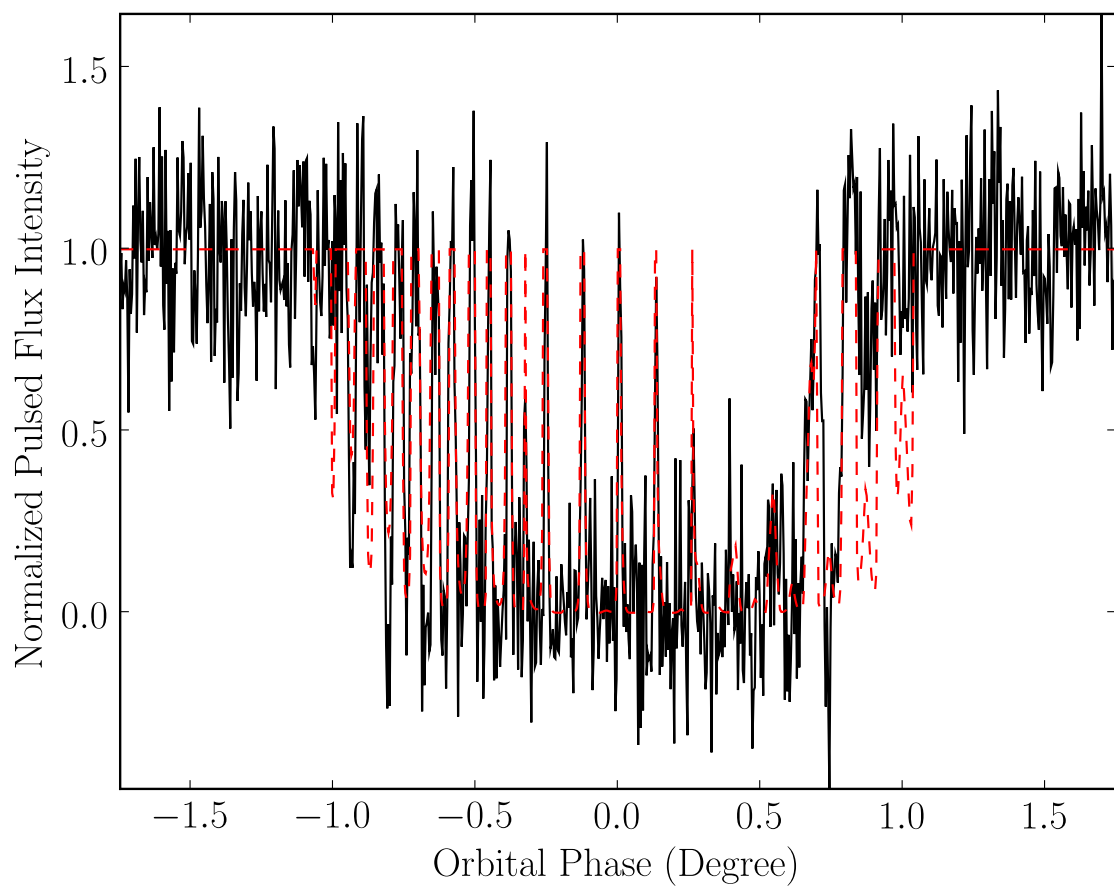


Fig. 3

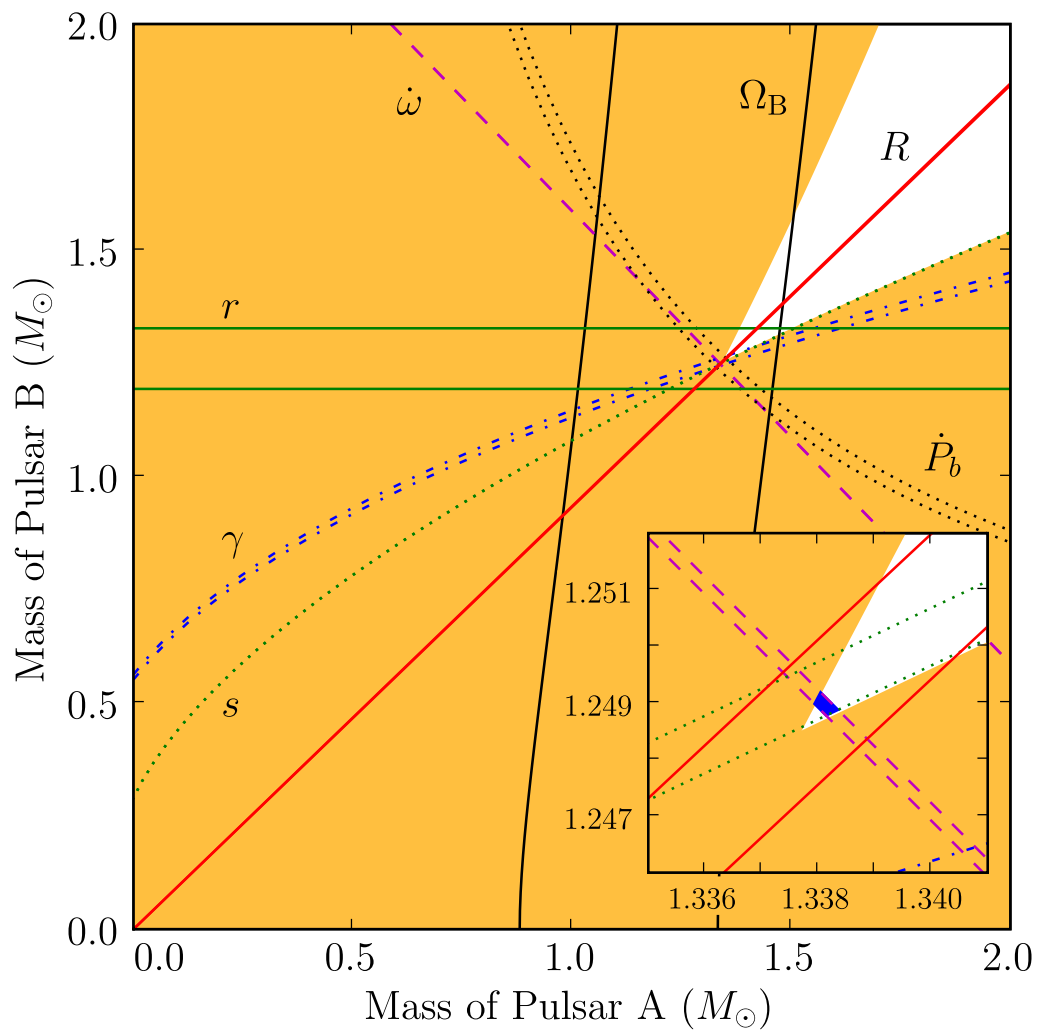


Fig. 4

Supporting Online Material

1 Eclipse Model

For the eclipse model we follow the prescription of (I), section 5.2, which proposes that the eclipses result from synchrotron absorption of relativistic electrons trapped in the truncated dipolar magnetic field of pulsar B. The intensity of the transmitted radio emission from pulsar A is calculated from the optical depth of pulsar B's magnetosphere, τ . For a given data point in the light curve, the optical depth is calculated as follows:

$$\tau = \mu \int_{-R_{\text{mag}}}^{R_{\text{mag}}} \left(\frac{B \sin \kappa}{B_{\text{mag}}} \right) d \left(\frac{x}{R_{\text{mag}}} \right), \quad (1)$$

where μ is a free parameter accounting for the characteristic optical depth of the magnetosphere at 820 MHz; x is the radial position along our line of sight in units of R_{mag} , the truncation radius of the dipole magnetosphere; B is the local magnetic dipolar field strength in units of B_{mag} , the strength at the truncation radius; and κ denotes the angle between our line of sight and the local direction of the magnetic field. Beyond the truncation radius, the optical depth is assumed to be zero. Pulsar B is at the origin of a coordinate system chosen so that x is along our line of sight, y is in the plane of the sky along the projected orbital motion and z is in the plane of the sky orthogonal to the $x - y$ plane (i.e. z is parallel to the projected angular orbital momentum). In this coordinate system the apparent motion of pulsar A is at a fixed value $z = z_0$. The orientation of the pulsar B spin axis can be described by two angles, θ the colatitude of the spin axis with respect to the z axis, and ϕ the longitude of the spin axis with respect to the $x - z$ plane. Finally, the inclination of the magnetic axis with respect to the spin axis of pulsar B is α (see Fig. 1 in the main article for a schematic view of the double pulsar showing the important model parameters).

Relativistic spin precession is expected to cause the spin angular momentum vector of pulsar

B to precess around the total angular momentum of the system, which we take to be the same as the orbital angular momentum since the spin contribution is negligible ($\sim 0.0001\%$). The time evolution of the pulsar spin axis in a coordinate system aligned with the orbital angular momentum is given by:

$$\delta = \delta_0, \quad (2)$$

$$\phi_{\text{so}} = \phi_{\text{so}0} - \Omega_B t, \quad (3)$$

where δ and ϕ_{so} are the colatitude and the longitude of the spin axis with respect to the total angular momentum, respectively (2). They are related to our coordinate system in the following way:

$$\cos \theta = \cos(90^\circ - i) \cos \delta - \sin(90^\circ - i) \sin \delta \cos \phi_{\text{so}}, \quad (4)$$

$$\sin \phi = \frac{\sin \delta \sin \phi_{\text{so}}}{\sin \theta}. \quad (5)$$

Because we observe the system almost perfectly edge-on ($i \approx 90^\circ$) the z axis and the total angular momentum are almost perfectly coincident. Hence, we can make the approximation $\theta \approx \delta$, and $\phi \approx \phi_{\text{so}}$. Therefore, the evolution of the spin geometry given by equations 2 and 3 holds in our coordinate system as well.

2 Eclipse Model Fitting

Our Bayesian fitting of the model to individual eclipse data involved the six free parameters introduced above: μ , z_0 , R_{mag} , α , θ and ϕ (see Fig. 1 in the main article for a schematic view of the model geometry). We assumed flat priors for all parameters and evaluated the joint posterior probability using a Markov Chain Monte Carlo (3) for the exploratory phase of the eclipse modelling. We coupled the Markov Chain Monte Carlo to simulated annealing (4) in the early stage of the chain to boost up convergence and explore the parameter space more efficiently. We ran

between three and five independent Markov Chains for each fit in order to check for consistency in the results. With this fitting optimization technique, we explored the full parameter sub-space corresponding to the geometric orientation of pulsar B’s magnetosphere (i.e. α , θ and ϕ) as well as enough of the other parameters to identify the best-fit values.

A quantitative treatment of changes in the eclipses requires incorporation of the eclipse model in a framework accounting for parameter evolution. Except for ϕ , we do not find any significant secular evolution of the model parameters from their marginal posterior probability (5). Indeed, theoretical considerations let us presume that only ϕ should change over time due to relativistic spin precession. The Markov Chain Monte Carlo technique poorly samples regions of low probability and so we fixed $\mu = 2$, $R_{\text{mag}} = 1.29^\circ$ (projected value in terms of orbital phase) and $z_0/R_{\text{mag}} = -0.543$, their best-fit values, before making a deeper investigation of pulsar B’s spin axis evolution. Although θ and α are not expected to vary, we did not fix them as they are highly covariant with ϕ , as opposed to the other parameters, but also because they contain valuable information about pulsar B’s geometry. Then, we completed our analysis of the eclipse evolution using a high resolution grid to map the now-reduced parameter space likelihood, containing three free parameters. Following equations 2 and 3, this analysis implements a Bayesian joint fit that assumes $\alpha = \alpha_0$ and $\theta = \theta_0$ are constant, and that ϕ linearly varies with time, i.e. $\phi = \phi_0 - \Omega_B t$, where Ω_B is the precession rate. The epoch of $\phi = \phi_0$ is May 2, 2006 (MJD 53857). Detailed results from this fit showing different combinations of one- and two-dimensional marginal posterior probabilities are presented in Fig. S1. Values reported in Table 1 of the main article were derived from these one-dimensional marginal posterior probability functions, assuming that the integrated probabilities are unity.

3 Analysis of Systematics

We investigated the importance of systematics in the eclipse modeling and concluded that two main effects should contribute to increasing the total uncertainty in our best-fit geometric parameters, above the statistical value. First, we observe considerable changes in the pulse profile of pulsar B as shown in Fig. S2. Since the spin phases of pulsar B are input data for the modeling, losing the fiducial reference to the neutron star surface will introduce additional error in the fitted eclipse parameters. While we do not require a measurement of the spin phases as accurate as for timing purposes, a few percent offset translates into slightly different geometrical parameters. The main effect of varying spin phases is to assign earlier or later rotational phases that mimic a slightly faster or slower precession rate. The pulse profile evolution of pulsar B is likely caused by the changing viewing geometry due to relativistic spin precession. Although it is not clear how pulsar B's pulse profile geometry is related to its surface, we are confident that the technique we used to determine the spin phases yields reliable results.

A second source of systematics arises from the choice of the eclipse region to include in the fit. Changes in the eclipse light curve due to relativistic spin precession are not uniform and the eclipse model tends to perform better toward the eclipse center than at the ingress or the egress. As opposed to the eclipse center, where our sight line to pulsar A goes deep inside and outside the magnetosphere of pulsar B as it rotates, our sight line only briefly intersects the edge of the magnetosphere at the beginning and the end of the eclipse. Therefore, local distortions of pulsar B's magnetic field or variations of the plasma density may give rise to a slight departure from our model. Indeed, we observe that fitting the whole eclipse does not generally provide qualitatively good fits. The narrow and periodic modulations in the eclipse center are very important markers for the geometric orientation of pulsar B but they tend to be misfitted because broader features in the egress region lead to larger variations of the goodness-of-fit. We find that excluding

the egress more accurately fits the overall light curves, without sacrificing critical information derived from narrow modulations, while still qualitatively reproducing the egress. Therefore, we chose to fit the eclipse in the range $[-1.0^\circ, 0.75^\circ]$ centered around conjunction (see Fig. 3 of the main article for an example of a fitted eclipse light curve).

Determining the boundaries of the region to fit is arbitrary and hence we estimated how much dispersion in the best-fit values is induced by other choices of limits. We compared our actual choice, $[-1.0^\circ, 0.75^\circ]$, with the full eclipse, $[-1.0^\circ, 1.0^\circ]$, the eclipse center, $[-0.6^\circ, 0.6^\circ]$, and the extended center, $[-0.7^\circ, 0.7^\circ]$, fits. In a Bayesian framework, we can easily incorporate the effect of systematics as priors on the model parameters. For simplicity and because the functional form of the systematics is poorly defined we assume Gaussian priors. Therefore, we can recast the posterior probability distribution of our pre-systematics analysis work, for which we were assuming constant priors:

$$p(\alpha, \theta, \phi | D) \propto \mathcal{L}(D | \alpha, \theta, \phi), \quad (6)$$

as:

$$p(\alpha, \theta, \phi | D) \propto \int_{\alpha'} \mathcal{N}(\alpha - \alpha', \sigma_\alpha) \int_{\theta'} \mathcal{N}(\theta - \theta', \sigma_\theta) \int_{\phi'} \mathcal{N}(\phi - \phi', \sigma_\phi) \mathcal{L}(D | \alpha', \theta', \phi') d\alpha' d\theta' d\phi', \quad (7)$$

where $\mathcal{N}(\nu, \sigma_\nu)$ is a Gaussian distribution of mean ν and standard deviation σ_ν . The likelihood, $\mathcal{L}(D | \alpha, \theta, \phi)$, is defined as $\exp(-\chi_\nu^2/2)$, with χ_ν^2 being the standard reduced chi-square. From the analysis of systematics due to the choice of the region to fit, along with the additional uncertainty in the spin phase of pulsar B due to the long-term pulse profile variations, we estimate that systematics contribute $\sigma_\alpha = 1^\circ$, $\sigma_\theta = 1^\circ$ and $\sigma_\phi = 2.0^\circ$. Note that incorporating Gaussian priors due to systematics has the effect of convolving the three-dimensional likelihood obtained from the eclipse fitting, $\mathcal{L}(D | \alpha, \theta, \phi)$, with a three-dimensional Gaussian. The analysis reported in this article includes these priors (this is particularly relevant for numbers quoted in Table 1 of

the main article and for the marginalized posterior probability distributions presented in Fig. S1 of this Supporting Online Material).

References and Notes

1. M. Lyutikov, C. Thompson, *ApJ* **634**, 1223 (2005).
2. T. Damour, J. H. Taylor, *Phys. Rev. D* **45**, 1840 (1992).
3. W. R. Gilks, *Markov Chain Monte Carlo in Practice* (Chapman & Hall/CRC, 1995).
4. S. Kirkpatrick, C. D. Gelatt, M. P. Vecchi, *Science* **220**, 671 (1983).
5. Marginalization is a common technique in Bayesian analysis that consists of integrating the joint posterior probability over the parameters that are not of interest so that it is reduced, in this case, to a one-dimensional probability for the parameter that we wish to consider (6).
6. P. C. Gregory, *Bayesian Logical Data Analysis for the Physical Sciences: A Comparative Approach with 'Mathematica' Support* (Cambridge University Press, Cambridge, UK, 2005).

Fig. S1 Pulsar B’s pulse profile consisting of the integrated flux at all orbital phases for each observation in our data set. Pulse profiles are normalized so the peak is unity and they are displayed with an incremental 1-unit vertical shift for clarity (the vertical axis does not show a linear time sequence). The vertical red dashed line marks the fiducial spin phase, which was determined by aligning the profiles using the first ten Fourier bins of the original 512-bin profile assuming that the two narrow peaks visible in the more recent data are the “edges” of an underlying unimodal envelope reminiscent of the profile in the earlier observations. Note that the observation length and radio interference contamination slightly varies from epoch to epoch but the overall signal-to-noise ratio decreases in the latest observations due to pulsar B becoming weaker. MJD 52996 corresponds to Dec. 23, 2003, and MJD 54430 to Nov. 26, 2007.

Fig. S2 One- and two-dimensional projections of the marginalized posterior probability distributions for the joint fit of the parameters’ evolution. Black contours in two-dimensional maps are joint 1, 2, 3, 4 and 5σ confidence regions, with the red color being associated with a higher likelihood value. The epoch of $\phi = \phi_0$ is May 2, 2006 (MJD 53857). Note that these probability distributions include priors related to systematic uncertainties (see Section 3 of this Supporting Online Material).

Movie S1¹ The eclipses in the double pulsar PSR J0737–3039A/B occur when pulsar A’s projected orbital motion, represented by a gray circle moving on a black line, passes behind its companion, pulsar B. Radio emission from pulsar A is absorbed via synchrotron resonance with the plasma trapped in the closed field lines of the truncated dipolar magnetosphere of pulsar B, shown as a colored dipolar structure. Since pulsar B’s magnetic dipole axis is misaligned with respect to its spin axis (represented by a diagonal rod), the opacity along our sight line to pulsar A varies as a function of pulsar B’s spin phase. The theoretical light curve resulting from the eclipse animated in the upper panel is drawn as a black curve in the bottom panel and real eclipse data, observed with the Green Bank Telescope in April 2007, are overlaid in red.

Movie S2¹ Time-lapse animation displaying the evolution of pulsar B’s geometry in the double pulsar PSR J0737–3039A/B due to relativistic spin precession between January 2004 and January 2029. The truncated dipolar magnetosphere of pulsar B, shown as a colored dipolar structure, rotates about its spin axis, pictured as a diagonal rod. The apparent orbital motion of pulsar A during the eclipse corresponds to the horizontal black line intersecting pulsar B’s magnetosphere. Relativistic spin precession is similar to the wobbling of a spinning top and induces a motion of the spin-axis orientation around the orbital angular momentum, which is vertical in this movie. The theoretical light curve corresponding to the eclipse animated in the upper panel is drawn in the lower panel. The angle ϕ corresponds to the longitude of the spin axis, with 0° being the direction coincident with the line of sight.

¹Movies, as well as the published version of this paper, can be found at <http://www.sciencemag.org/cgi/content/full/sci;321/5885/104/DC1>.

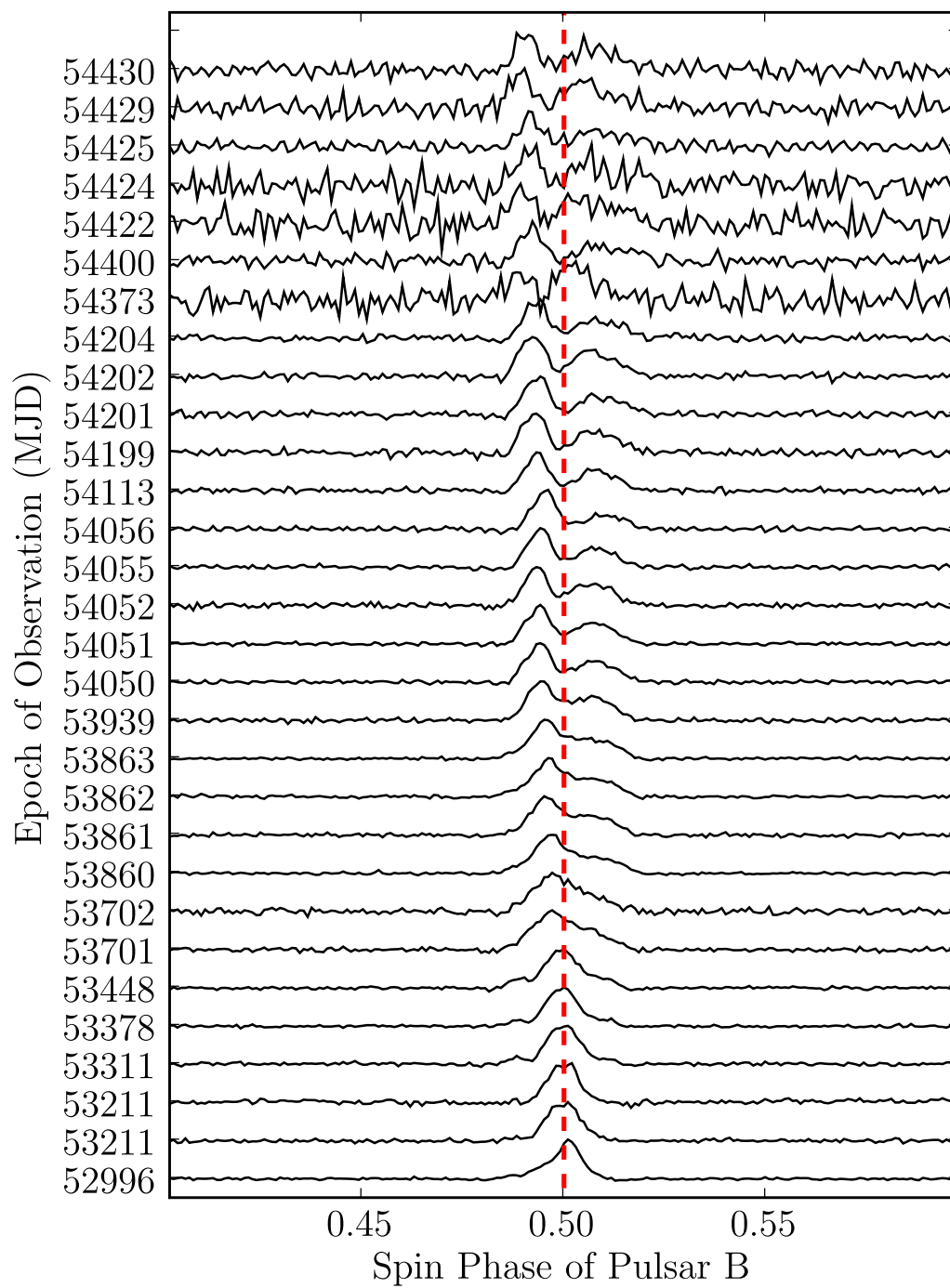


Fig. S1

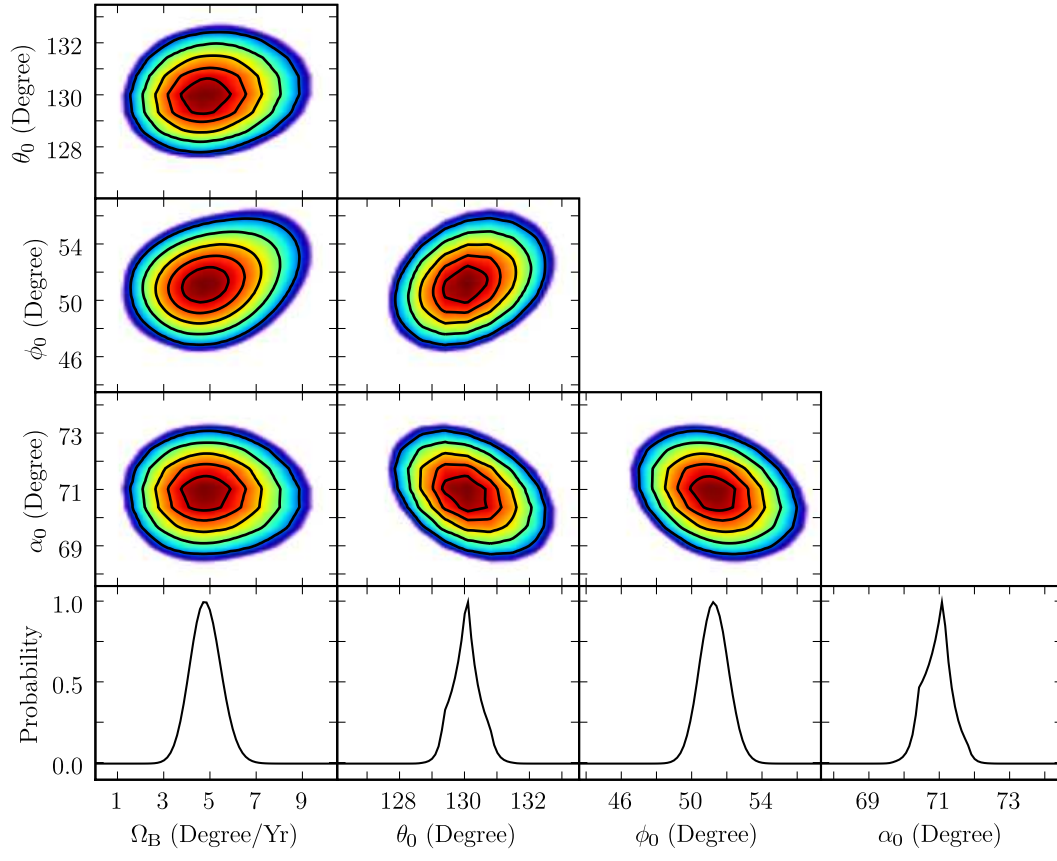


Fig. S2